ADVANCED MATERIALS
www.advmat.de

# Deterministic Fabrication and Quantum-Well Modulation of Phase-Pure 2D Perovskite Heterostructures for Encrypted Light Communication

*Enliu Hong, Ziqing Li,* Xinyu Zhang, Xueshuo Fan, and Xiaosheng Fang**

**Deterministic integration of phase-pure Ruddlesden–Popper (RP) perovskites has great significance for realizing functional optoelectronic devices. However, precise fabrications of artificial perovskite heterostructures with pristine interfaces and rational design over electronic structure configurations remain a challenge. Here, the controllable synthesis of large-area ultrathin single-crystalline RP perovskite nanosheets and the deterministic fabrication of arbitrary 2D vertical perovskite heterostructures are reported. The 2D heterostructures exhibit intriguing dual-peak emission phenomenon and dual-band photoresponse characteristic. Importantly, the interlayer energy transfer behaviors from wide-bandgap component to narrow-bandgap component modulated by comprising quantum wells are thoroughly revealed. Functional nanoscale photodetectors are further constructed based on the 2D heterostructures. Moreover, by combining the modulated dual-band photoresponse characteristic with double-beam irradiation modes, and introducing an encryption algorithm mechanism, a light communication system with high security and reliability is achieved. This work can greatly promote the development of heterogeneous integration technologies of 2D perovskites, and could provide a competitive candidate for advanced integrated optoelectronics.**

## 1. Introduction

The advent of Big Data era has led to a continuous surge in the amount of information that necessitates daily processing and transmission, thereby putting forward higher requirements for the reliability and encryption of communication systems. Compared with traditional communication systems, light communication system using lasers with specific wavelengths as information carriers and the atmosphere as communication medium offers numerous advantages, such as large data transmission capacity, ultrafast transmission speed, robust resistance against electromagnetic interference, and high reliability,[1–3] which is more suitable for meeting the requirements of modern large-scale data communication. Nevertheless, there are also problems such as important data being stolen or tampered with in the transmission process,[4,5] thus how to improve the security of light communication system is the focus of research communities. It is well known that photodetectors (PDs) that convert light input to electric signals are ideally suited devices for optical communication systems.[6–8] In particular, functional PDs based on rational-designed 2D van der Waals heterostructures (2D vdWHs) have demonstrated great potential in the fields of light communication, thermal imaging, military monitoring, and so forth,[9–11] among which the light communication technique arouses widespread attention as the medium of light signals and data information. Therefore, developing nanoscale functional PDs for secure light communication is very essential.

In recent years, 2D vdWHs have attracted enormous attention owing to their superior properties, such as high conductivity, broad light absorption, high carrier mobility, tunable interlayer excitons,[12–15] and so on. Normally, mechanical stacking is used to form 2D vdWHs, the as-prepared heterostructures can overcome the restriction of lattice matching and exhibit greatly improved interface quality,[16] thereby enabling unlimited combinations of different 2D layers. The degree of freedom offered by this method tremendously expands the 2D vdWHs family in an endless way. By definition, the fabrication of 2D vdWHs requires two or more different 2D materials, which have been intensively studied recently. To date, more than a hundred kinds of 2D materials have been developed by various synthetic methods in the last decade and the number is still continuously growing,[17] typically including graphene, transition metal dichalcogenides, hexagonal boron nitride (h-BN), black phosphorus (BP), MXenes, layered

---

E. Hong, X. Zhang, X. Fan, X. Fang
Department of Materials Science
State Key Laboratory of Molecular Engineering of Polymers
Fudan University
Shanghai 200433, P. R. China
E-mail: xshfang@fudan.edu.cn
Z. Li, X. Fang
Shanghai Frontiers Science Research Base of Intelligent Optoelectronics and Perception
Institute of Optoelectronics
Fudan University
Shanghai 200433, P. R. China
E-mail: lzq@fudan.edu.cn

The ORCID identification number(s) for the author(s) of this article can be found under https://doi.org/10.1002/adma.202400365

**DOI: 10.1002/adma.202400365**

perovskites, etc. Among numerous 2D materials, Ruddlesden–Popper (RP) halide perovskites have standout under the spotlight by virtue of their exceptional physical and optoelectronic properties, such as large exciton binding energy,[18] long carrier diffusion length,[19] adjustable bandgap,[20] enhanced stability,[21] and thus are considered as competitive candidates for next-generation optoelectronic devices. Unlike their 3D counterparts, 2D RP perovskites own a soft lattice and natural quantum well structure,[22,23] allowing them to be stacked layer by layer to obtain desired optical and optoelectronic properties, thus fulling the promises of 2D perovskite heterostructures for potential applications. The rational design of 2D perovskite heterostructures for functional PDs applied in light communication system, however, demands high-quality single-crystalline perovskites and controllable fabrication capability to achieve the desired electronic structures. In addition, although there have been some reports of 2D perovskite heterostructures, the rich physical electronics in them are still largely unexplored, especially how the energy band modulation effect affects carrier generation, separation, transportation, and recombination, which holds great significance for applications discovery.

Herein, the controllable synthesis of single-crystalline phase-pure RP perovskite nanosheets and the deterministic fabrication of arbitrary vertical 2D perovskite heterostructures are reported. The optical and optoelectronic properties of as-fabricated heterostructures are systematically investigated, in particular revealing the dual-peak emission phenomenon and the selectively modulated optoelectronic response characteristic of $(BA)_2PbBr_4/(BA)_2PbI_4$ caused by type-I band alignment. Moreover, a customized encryption algorithm is proposed to address the communication security issue. By virtue of this novel mechanism, the transmitted data could be transformed and disguised in a certain form in advance, so that unauthorized users cannot understand the true meaning of the original information behind the transmitted data. Combining the modulated dual-band photoresponse characteristic with encryption algorithm mechanism and double-beam irradiation modes, heterojunction-based functional nanoscale PDs for secure light communication are achieved. Our work demonstrates the artificial integration of 2D RP perovskite heterostructures with designed electronic structure configurations for advanced functional and miniaturized PDs, providing competitive options for encrypted light communication.

## 2. Results and Discussion

As a matter of fact, it is still a challenge to obtain large-area (>100 µm) pure-phase 2D perovskite single crystals (PSCs), which is fundamental for the construction of high-quality heterostructures. Here, the single-crystalline 2D RP perovskite nanosheets were synthesized using the reported liquid-air interface floating growth method,[24,25] which is illustrated in detail in Figure S1, Supporting Information. Benefiting from the solution processability of perovskites, we observed their freestanding self-assembly behaviors at the liquid-air interface, by virtue of which various high-quality 2D RP PSCs can be prepared. Three kinds of representative as-synthesized nanosheets with compositions of $(BA)_2PbBr_4$ (BPB), $(BA)_2(MA)Pb_2Br_7$ (BMPB), and $(BA)_2PbI_4$ (BPI) are shown in **Figure** 1a,b,c, respectively, and the transparent and pink substrates are PDMS and $Si/SiO_2$, respectively. It can be seen that all nanosheets display high crystallinity with regular shapes and clean surfaces under both bright/dark fields. And in the view of scanning electron microscope (SEM) shown in Figure S2, Supporting Information, clear boundaries and smooth surfaces can be obviously observed, further demonstrating the high quality of the obtained nanosheets. Compared with mechanically exfoliated flakes of RP perovskites, these directly-grown nanosheets without torn pieces and residual particles have obvious advantages for further treatments. The thicknesses of these PSCs are revealed by height profiles in Figure S3, Supporting Information, specifically, 40 nm for BPB, 115 nm for BMPB, and 100 nm for BPI. Correspondingly, their photoluminescence (PL) spectra are presented in Figure 1d–f, by which their compositions and phase-purity characteristics are further confirmed. Concretely, the PL feature positions are 412, 440, and 520 nm for BPB, BMPB, and BPI, respectively, which agree well with previous studies.[26–28] The sharp and strong PL peaks indicate the high crystalline quality of these PSCs with few trap density and defects. It is well known that the full width at half maximum (FWHM) could qualitatively reflect the materials' crystallinity of the same system.[29–31] Notably, the hexagonal BPB single crystals with ultrathin thickness of 40 nm exhibit an ultra-narrow FWHM of 8 nm, which is much narrower than previous reports,[32,33] indicating their much higher crystalline quality with lower carrier scattering and less nonradiative recombination.

The controllable synthesis of high-quality 2D RP perovskite nanosheets lays a foundation for the construction of 2D perovskite vertical vdWHs. These directly-grown perovskite nanosheets with clean and smooth surfaces are perfect platforms to construct intimate heterojunctions for desired electronic structures. As depicted in Figure 1g, with the help of the PDMS-assisted dry transfer technique, deterministic fabrication of arbitrary 2D perovskite heterostructures is achieved via successive mechanical stacking process. Based on three kinds of the phase-pure perovskite nanosheets, we construct two representative 2D vertical RP perovskite heterostructures BPI/BPB (hetero-1, **Figure** 2a) and BPB/BMPB (hetero-2, Figure 2b). Schematics and height profiles of the as-constructed vertical heterostructures are displayed in Figure 2c,d, from which the crystal structures and thicknesses of each component phase can be clearly seen.

As shown in Figure 2a(i),b(i), both hetero-1 and hetero-2 exhibit clear interface and appressed contact, demonstrating the valid integration of nanosheets after stacking. The soft crystal lattice feature of RP perovskites ensures the forming of high-quality interfaces. The height profiles in Figure 2c(ii),d(ii) clearly show the thicknesses of each component and junction area, verifying the heterostructures fabrication process. The surface morphology and 3D configurations are confirmed by atomic force microscopy (AFM) and confocal laser scanning microscopy (LSM). The AFM images (Figures 2a(ii) and S4a(ii), Supporting Information) indicate a highly smooth surface with a minimal roughness of only 0.9 nm, as well as a sharp step in the heterointerface region of hetero-1. The LSM images (Figures 2b(ii) and S4b(ii), Supporting Information) reveal the ideal integration of BPB and BMPB after stacking. The color contrast in the view of AFM and LSM is attributed to the thickness differences. The above results indicate that we have achieved the deterministic construction of high-quality heterogeneous interfaces. Moreover, the optical properties of as-constructed heterostructures are further

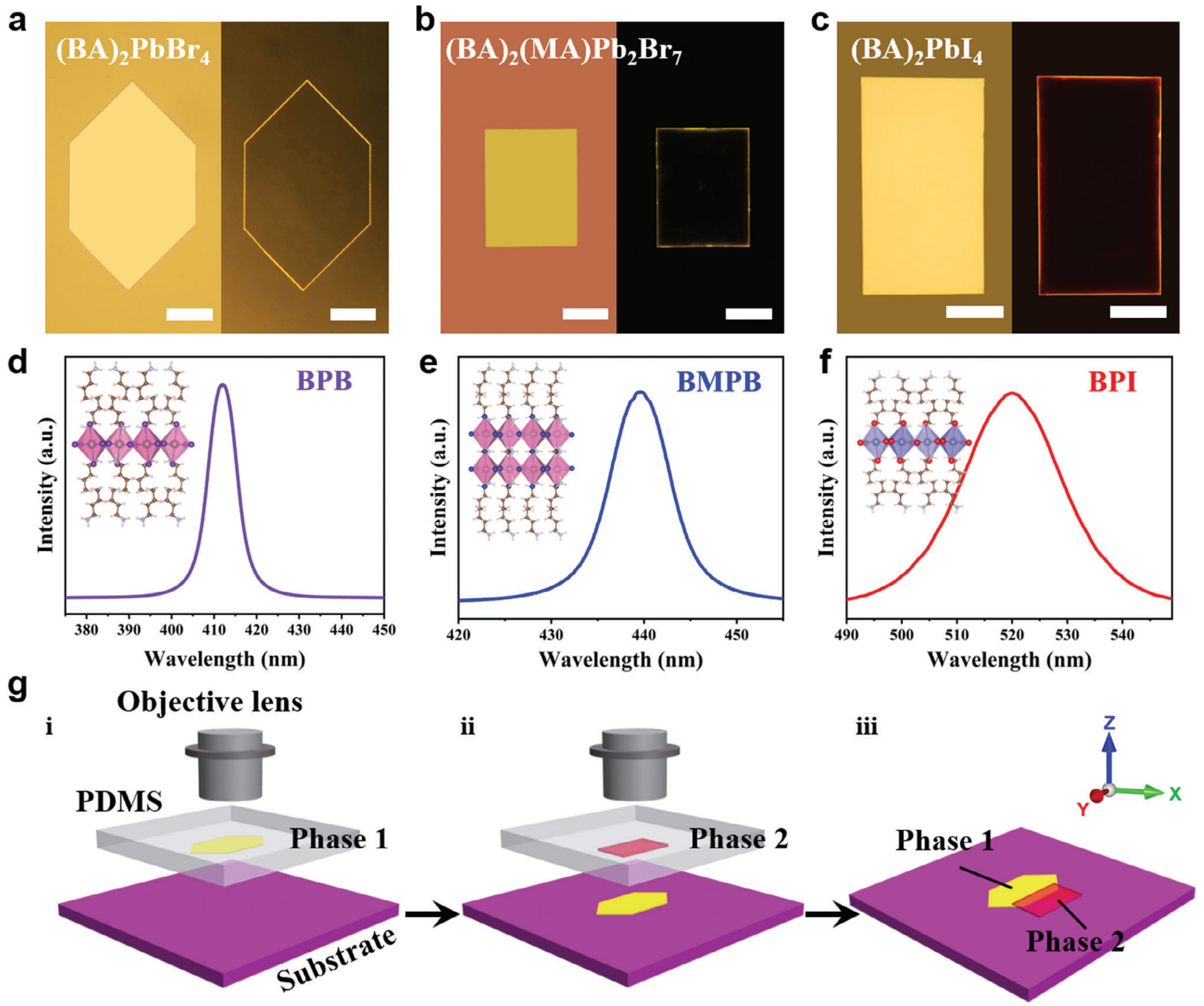

**Figure 1.** The optical microscope images of three representative as-grown PSCs (left/right: bright field/dark field. Scale bar: 50 µm). a) $(BA)_2PbBr_4$ (BPB). b) $(BA)_2(MA)Pb_2Br_7$ (BMPB). c) $(BA)_2PbI_4$ (BPI). And their corresponding PL spectra (inset: crystal structures depictions) d) BPB, peak position at 412 nm. e) BMPB, peak position at 440 nm. f) BPI, peak position at 520 nm. g) Deterministic fabrication process of 2D perovskite heterostructures. i) Transferring PSCs of phase 1 onto target substrate under the objective lens. ii) Stacking another nanosheet of phase 2 to phase 1 with precise control over alignment. iii) Constructed heterostructures made by two-component phases.

investigated by PL measurements (Figure 2a(iii),b(iii)), from which the obvious dual-peak emission phenomenon can be seen. Specifically, the PL spectra collected on the heterojunction areas show dual peaks at 411 nm and 521 nm for hetero-1, and at 413 and 440 nm for hetero-2, respectively, basically consistent with the positions of individual pristine perovskite phases, illustrating negligible ion migration in heterojunction regions, which is beneficial for the stability of heterojunction-based devices. Normally, halogen anion diffusion usually occurs at the interface, leading to PL peaks shift and device failure, which is undesirable.[34–36] The 2D perovskite heterostructures here do not have such problem, probably because the unique long-chain organic alkylamine cations of RP perovskites act as migration barriers to impede halogen diffusion. And it is worth noting that the relative PL intensity of hetero-1 exhibits a significant disparity after the heterogeneous integration process, the intensity of BPI is greatly enhanced while that of BPB is obviously weakened. We ascribe this phenomenon to the energy transfer from wide-bandgap component (WBC) to narrow-bandgap component (NBC) due to type-I band alignment (illustrated in Figure 2a(iv)). In this case, the photogenerated carriers (electron-hole pairs) of the WBC will transmit to the lower energy levels of the NBC, where electrons and holes will aggregate at the conduction band minimum and valence band maximum of the NBC, respectively. Thus, the recombination of electron-hole pairs in WBC is significantly inhibited while that of the NBC is greatly enhanced. In the situation of type-II band alignment (hetero-2, Figure 2b(iv)), the electrons and holes effectively separate and transport in a circular pathway, thereby inhibiting the carrier recombination process and producing negligible influence on the PL intensity, which

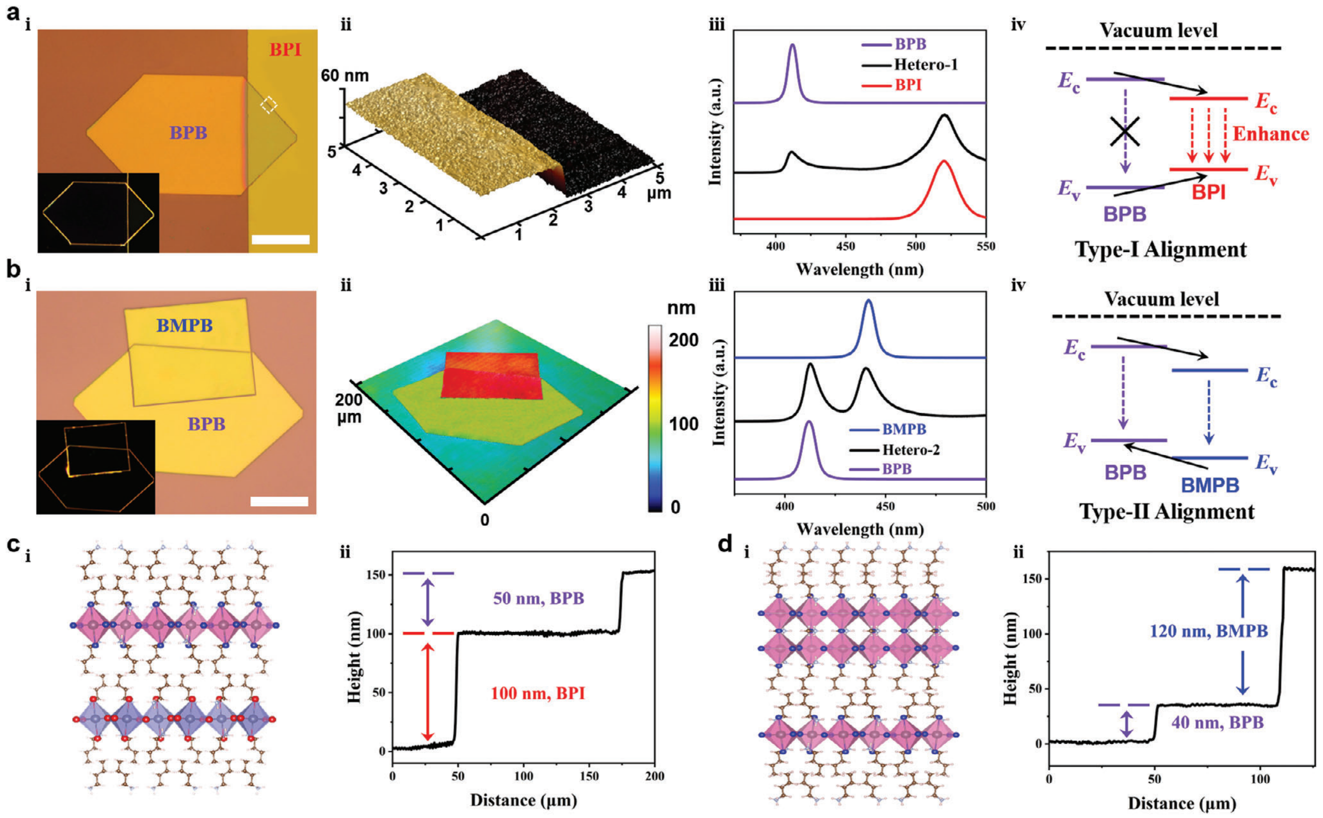

**Figure 2.** Characterizations of the as-fabricated 2D vertical RP perovskite heterostructures. a) Hetero-1. i) Optical image on a Si/SiO$_2$ substrate. The inset shows the corresponding image under dark field. Scale bar: 50 µm. ii) AFM 3D image of the selective white-dash area. iii) Normalized confocal PL spectra (offset for visibility) taken over the respective regions. iv) Type-I band alignment of the hetero-1. b) Hetero-2. i) Optical image on a Si/SiO$_2$ substrate. Scale bar: 50 µm. ii) Corresponding LSM 3D image. iii) Normalized confocal PL spectra (offset for visibility) taken over the respective regions. iv) Type-II band alignment of the hetero-2. c,d) i) Schematic illustrations and ii) height profiles of the hetero-1 and hetero-2.

are consistent with the experimental results. These findings not only validate the universal feasibility of deterministic fabrication of high-quality 2D vertical perovskite heterostructures, but also investigate and verify the intriguing physical photonics properties of the novel perovskite heterostructures.

In order to further explore the potential applications of these single-crystalline perovskites, we first investigate the optoelectronic properties of these single components by constructing PDs. The device structure is shown in **Figure 3a** and the carriers transport model is depicted in Figure 3b. In fact, electron-hole pairs are generated by laser excitation, followed by their subsequent separation and transportation to the drain and source electrodes to produce photocurrent. As seen in Figure 3c–e, the performance of three components displays variations in terms of dark current, photocurrent, and the optimal response wavelength. Specifically, the best wavelengths are 490 nm for BPI, 370 nm for BPB, and 390 nm for BMPB, respectively. At the same 3 V bias, the on/off ratios of BPI, BPB, and BMPB reach 1.8, 2.6, and 2.8 orders of magnitude, respectively. Based on these impressive results, dual-band (visible light + UV) photoresponse is expected to be achieved in the heterostructure-based PDs.

Considering that the BPB component has much thinner thickness and deeper optimal UV response characteristic, we focus on the hetero-1 to realize reasonable energy band alignment and ideal device structure. The diagram of the planar PD structure based on hetero-1 is depicted in **Figure 4a**. Correspondingly, the optical image of a real device is shown in Figure 4b. Benefiting from the favorable surface morphology of single-crystalline nanosheets with high flatness and cleanness, both ends of hetero-1 are in good contact with Au electrodes, and the heterogeneous region is closely fitted to form a high-quality junction interface, thereby constructing a planar 2D vdWHs PD.

Moreover, we selectively choose three specific points marked as 1, 2, 3, 4, and 5 in Figure 4b for conducting PL tests. The result in Figure 4d indicates that point 1 exhibits the highest strength, while point 3 demonstrates the weakest intensity, which suggests a positive correlation between proximity to the junction center area and an increase in PL intensity. In the same heterojunction region, the intensity disparity between points 1 and 2 is caused by warping edges, which means the interface is not tight enough at edges and leads to the PL intensity of edge area lower than the center area. In the center area, the scans of points 1, 4, and 5 display roughly the same result, indicating the homogeneity of the heterojunction. Due to the type-I energy band alignment, the PL signal intensity of NBC in heterojunction is much stronger than before (consistent with Figure 2a(iii)), this obvious enhancement indicates the efficient electron-hole recombination process and inefficient separation and transport process at the heterojunction interface. Kelvin probe force microscopy (KPFM) is further used to determine the energy band structure and contact potential

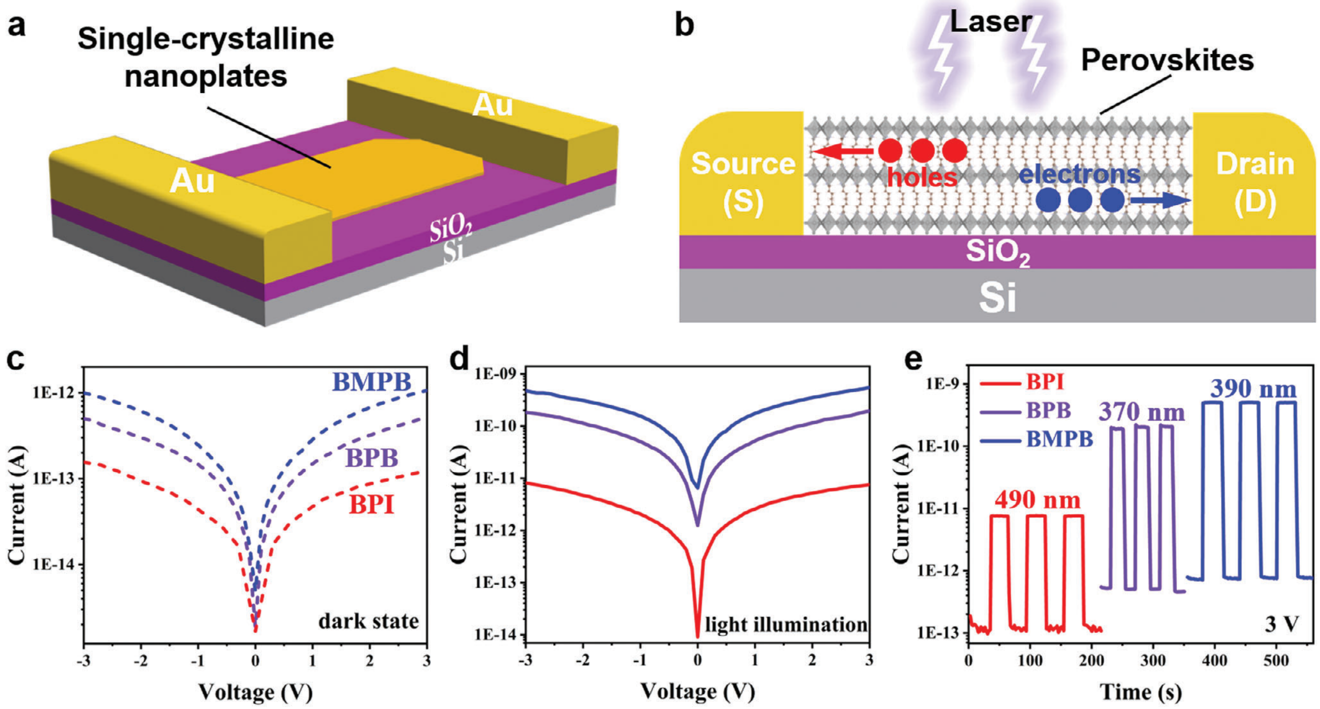

**Figure 3.** Optoelectronic performance comparison of 2D single-crystalline nanosheets PDs. a) Schematic of the Au-perovskites-Au device structure. b) Photo-generated carriers transport model of perovskites-based PDs. c,d) Semilogarithmic *I*–*V* curves in the dark state and under light illumination. e) Semilogarithmic *I*–*t* curves at 3 V bias, BPI, BPB, BMPB, respectively.

difference of the heterojunction. From the red dash line profile of surface potential and potential distribution in Figure 4c and Figure S5, Supporting Information, the Fermi level of BPB is determined to be about 110 meV higher than BPI. Combining with previously reported literatures,[37,38] the energy band alignment diagram is drawn in Figure 4g, which belongs to a typical type-I heterostructure. Furthermore, the optoelectronic properties of the Au-hetero1-Au planar PD are investigated. As expected, the dual-band photoresponse characteristic is observed (Figures S6 and S7, Supporting Information) and an interesting selective modulation effect caused by type-I band edge bending is revealed. As shown in Figure 4f, the hetero1-based PD not only inherits the excellent properties of low dark current from BPI and high photocurrent from BPB, but also amplifies this characteristic, resulting in the on/off ratio response at 370 nm reaches up to 3.9 orders of magnitude, which is 20 times higher than before. In order to avoid inaccuracy of the comparison caused by thickness inconsistency, nanosheets with the same thickness of ≈50 nm are chosen to fabricate PDs. Additionally, the *I*–*V* curves in Figure 4e demonstrate the existence of a built-in electric field within the heterojunction, resulting in a leftward shift of the curves. Because of the electric field and weak rectification effect, the current at −3 V seems like an unsaturated state. The 2D heterostructures constructed by vdWs usually give rise to an electric potential difference at the contact surface due to the different energy band structures of the two constituents, leading the forming of an internal electric field and subsequent electrons redistribution within materials. Meanwhile, the presence of the built-in electric field can effectively suppress the dark current noise and carrier recombination, thereby improving the photocurrent and photoresponse. Interestingly, although the photoresponse of hetero-1 is enhanced at 370 nm, the performance is weaker at 490 nm than before. By virtue of the type-I energy band alignment diagrams depicted in Figure 4h,i, the internal mechanism of energy band modulation effect can be comprehended. Under light illumination condition, the photogenerated electron-hole pairs separate and transport efficiently driven by the built-in electric field. The transport flow of carriers induces changes in concentration and electron barriers, leading to the blending of energy bands and facilitating electron injection and photoconductive gain. Under 370 nm light illumination, the WBC in type-I structure acts as a potential barrier, effectively confining the photogenerated carriers to the NBC as a potential well. The electrons and holes move oppositely driven by the built-in electric field. The holes transit the heterointerface without any block barriers, while the electrons are blocked by the conductive band offset and gather at the NBC side. In this situation, the recombination of electron-hole pairs in WBC is significantly inhibited and the carrier collection efficiency is greatly improved, thereby enhancing the optoelectronic properties of the WBC. Meanwhile, the carrier recombination on the NBC side is intensified, resulting in diminished performance and heightened PL strength, as evidenced by experimental results (Figure 4d,f). In case of 490 nm irradiation (Figure 4i), the interband absorption of WBC is negligible and the NBC could be considered as the only photoactive layer. Nevertheless, the transition electrons in NBC side are blocked by the bandedge offset, resulting in impaired performance. The slight response can be attributed to the existence of a few defect

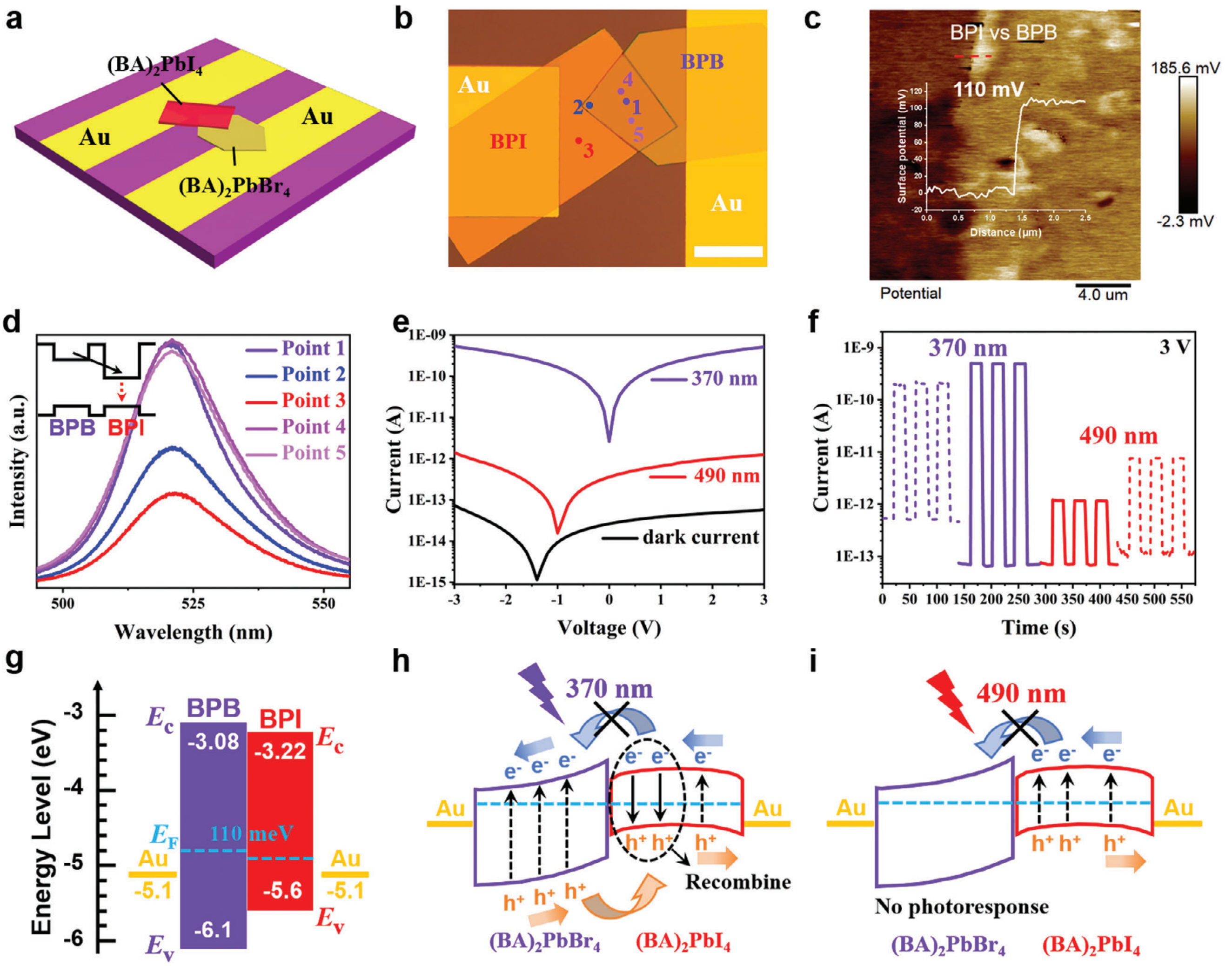

**Figure 4.** a) Schematic diagram of the heterojunction-based device structure. b) Optical image of a typical hetero-1 PD device. Scale bar: 50 µm. c) KPFM characterization of the BPB/BPI heterostructure. d) Confocal PL spectra collected in different points labeled in b, the inset shows the simplified band energy diagram of the two phases. e) *I*–*V* curves of the device after modulation. f) *I*–*t* curves at 3 V bias, the dash lines are the data of corresponding single component before modulation. g) Energy band structures of BPB and BPI before contact. h,i) Type-I energy band alignment diagrams of hetero-1 under 370 and 490 nm illumination, respectively.

states in WBC, thus establishing a coherent pathway for electron transport. This selective modulation effect of 2D perovskite heterostructures induced by type-I energy band alignment can be applied in functional PDs with rational design over their electronic structures.

The impressive modulated dual-band photoresponse capacity empowers the device for secure light communication. As seen in **Figure** 5a, the encrypted light communication system is achieved by combining double-beam irradiation modes and encryption algorithm mechanism. By simultaneously tuning the laser sources to on/off states, four illumination modes of signal inputs are formed, denoted as 00, 01, 10, and 11, respectively. Consequently, the data to be protected (plaintext, PT) can be transmitted in disguised forms (ciphertext, CT), and then digital signals carrying concrete information are output. The conversion between PT and CT requires a secret key (K) to complete the encryption and decryption process. Essentially, the K which can be used reversibly is a one-to-one correspondence relationship between letters and four-digit binary numbers, and this relationship can be randomly generated by the algorithm in real time and has high confidentiality. According to the randomly generated K, the PT can be encrypted, transmitted, and decrypted safely. Specifically, the PT is converted to a string of four-digit binary numbers using K, and then transmitted via the modulated dual-band photoresponse PD. Subsequently, the receivers decrypt the received signals using the same K to accomplish the entire process of light communication. Steady *I*–*t* curves are conducted with 365 and 490 nm light on-off to demonstrate the photoresponse characteristics in this device. As the light is illuminated at BPB-only area, 365 nm light can stimulate the device to output a current exceeding $10^{-10}$ A, whereas 490 nm light can only stimulate the area to a negligible photoresponse (Figure 5b). Similarly, when solely illuminating the BPI area, the area only response to the 490 nm light rather than 365 nm (Figure 5c). By contrast, as shown in Figure 5d, the

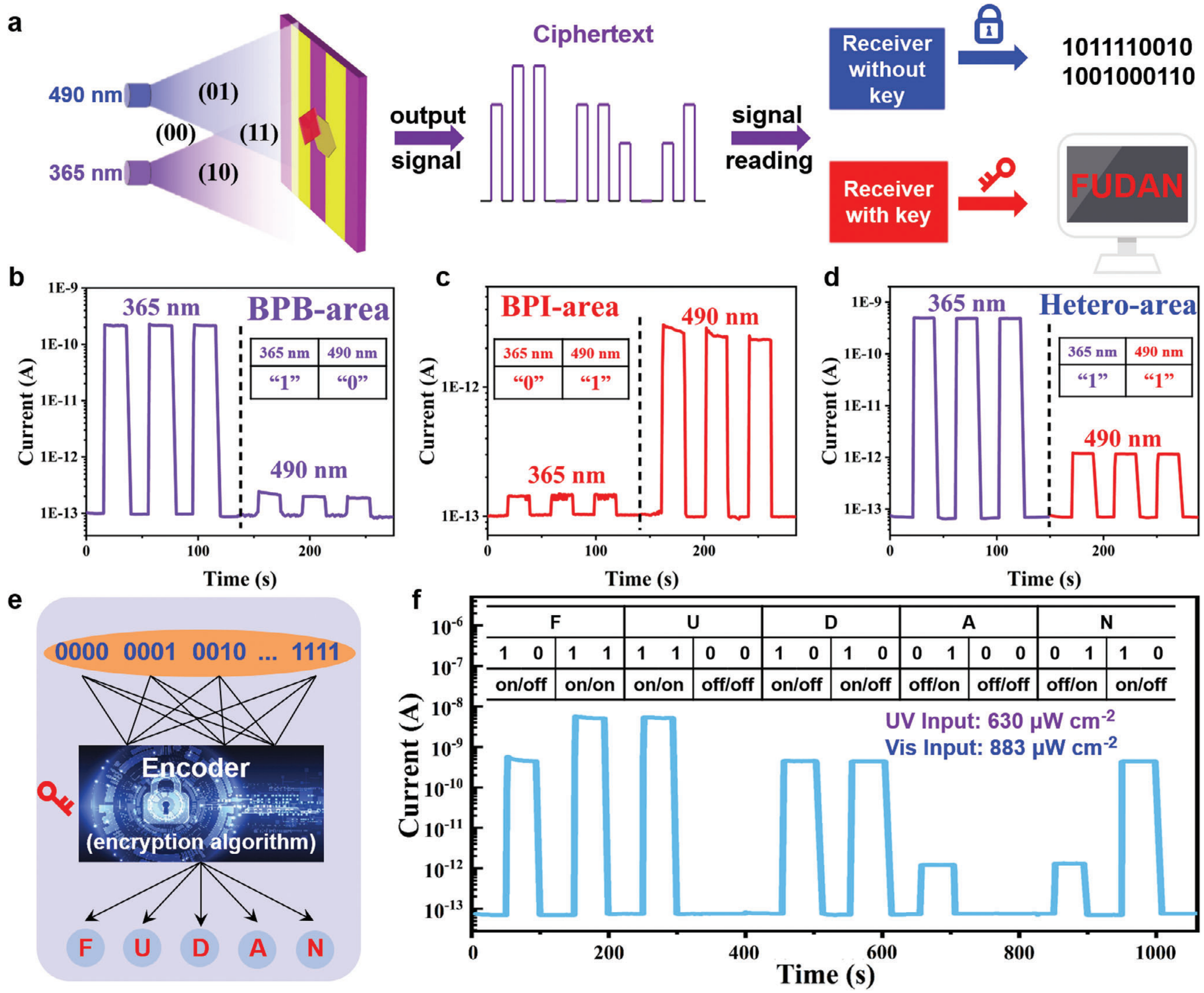

**Figure 5.** a) Schematic drawing of the light communication system of the BPI/BPB vdWHs device. b–d) *I*–*t* curves at 3 V bias, at different irradiated areas. e) The secret key generation mechanism by the encryption algorithm. f) The practical output two-byte signals of "10111100101001000110" generated by double-beam irradiation modes.

heterojunction region can respond to both 365 and 490 nm light. Experimentally, the 365 nm UV and 490 nm visible radiations with intensity of 630 and 883 μW cm$^{-1}$ respectively are employed as the signals' input source. Benefiting from the modulated dual-band photoresponse, these four types of incident modes are facile to be distinguished by the gradient photocurrent, and the photocurrent signal generated when UV and visible light are separately illuminated is defined as "10" and "01," respectively. As a demonstration, if we want to deliver the "FUDAN" message, we first dived this message into "F," "U," "D," "A," "N" five letters and convert them to four-digit binary numbers by the designed encryption algorithm (Figure 5e and Figure S8, Supporting Information). In this manner, the message is transformed into a string consisting of 20 binary digits of "10111100101001000110" and facilely delivered through the modulated dual-band photoresponse PD. As displayed in Figure 5f, the practical output verifies the feasibility and stability of the light communication system. For receivers who possess the K, they can decrypt the digital signals without any obstruction and obtain the actual message smoothly. On the contrary, even if an attacker without the K intercepts the transmission signal, he can only decode out a string of meaningless numbers. Additionally, the security can be further enhanced by increasing the bits of binary numbers, thereby exponentially increasing the time required for brute-force cracking to steal the encrypted information. The above results demonstrated the robustness of the designed light communication system in ensuring transmission security, making it highly suitable and reliable for efficient large-scale data transfer with significant potential for diverse applications.

## 3. Conclusion

In summary, we have successfully assembled pure RP perovskite phases with high-quality interfaces and structural diversity by deterministic fabrication method, thus realizing rational design over their electronic structures for light communication applications. The BPB/BPI heterostructure-based PD exhibits excellent performance with modulated dual-band photoresponse characteristic caused by type-I energy band alignment, which displays interlayer energy transfer behaviors. Based on this quantum-well modulation effect, the dark current is decreased and the photocurrent is improved, thus the on/off ratio is enhanced by 20 times. By combining the modulated dual-band photoresponse characteristic with double-beam irradiation modes, and introducing self-customized encryption algorithm mechanism, the secure light communication system with high reliability based on the heterojunction-based functional PDs is achieved. The in-depth exploration of exciton physics of this work could provide theoretical guidance for device constructions, and this deterministic fabrication work of arbitrary vertical 2D perovskite heterostructures holds great potential for developing advanced functional optoelectronics.

## 4. Experimental Section

*Materials*: BAI (99.9%), BABr (99.9%), MABr (99.9%), $PbI_2$ (≥98%), $PbBr_2$ (99.999%), Hydroiodic acid (HI, 55.0–58.0% in $H_2O$, contains 1.5% $H_3PO_2$ as stabilizer) and hydrobromic acid (HBr, 48 wt% in $H_2O$, 99.99%) were used as received without further treatment.

*Deterministic Fabrication Process*: The phase-pure perovskite single crystals were first obtained at the liquid-air interfaces, induced by surface tension. Then, the deterministic fabrication of 2D vertical perovskite heterostructures was achieved by a careful successive mechanical stacking process. Owning to an excessive temperature will cause the PDMS to expand too fast, thus to avoid any crack and damage to the single-crystalline nanoplates, it was suggested that the heating temperature was not more than 90 °C during the PDMS pick up-release step. The bottom Au electrodes were patterned by standard photolithography process, then 10 nm Cr and 50 nm Au were fabricated in turn through thermal evaporation.

*Characterizations*: The optical images were captured by Olympus microscope. PL spectra were acquired by Renishaw inVia-Qontor Raman microscope equipped with 325 and 532 nm lasers. The thickness profiles were tested by a step profiler (KLA-Tencor) and AFM (Bruker-Dimension Edge). The heterogeneous architecture was completed by a low-dimensional materials transfer platform (Metatest, E1-T). The surface morphology and 3D configurations were observed by SEM (Zeiss Sigma 300) and LSM (Zeiss LSM 900). The surface potential and potential distribution data were obtained by KPFM (Bruker-Dimension Icon). The optoelectronic properties were collected using the semiconductor characterization system (Keithley 4200-SCS) connected to a vacuum probe station (Lake Shore). A 75 W Xe lamp equipped with a monochromator and a 365 nm laser were used as light sources. The light density was measured by a NOVA II power meter (OPHIR photonics). All the tests were performed at ambient environment, that is, room temperature and atmospheric pressure.

## Supporting Information

Supporting Information is available from the Wiley Online Library or from the author.

## Acknowledgements

This work was financially supported by the National Natural Science Foundation of China (Nos 62374035, 62204047, 92263106, and 12211530438) and the Science and Technology Commission of Shanghai Municipality (No. 21520712600 and 19520744300).

## Conflict of Interest

The authors declare no conflict of interest.

## Data Availability Statement

The data that support the findings of this study are available from the corresponding author upon reasonable request.

## Keywords

2D perovskite heterostructures, dual-band photoresponse, dual-peak emission, encrypted light communication, quantum wells

Received: January 8, 2024
Revised: May 10, 2024
Published online:

[1] S. Liu, S. J. Jiao, Y. Zhao, H. L. Lu, S. Yang, D. B. Wang, S. Y. Gao, J. Z. Wang, L. C. Zhao, *Adv. Opt. Mater.* **2023**, *11*, 2300831.
[2] S. SeyedinNavadeh, M. Milanizadeh, F. Zanetto, G. Ferrari, M. Sampietro, M. Sorel, D. A. B. Miller, A. Melloni, F. Morichetti, *Nat. Photonics* **2024**, *18*, 149.
[3] F. Cao, Z. Li, X. Liu, Z. Shi, X. S. Fang, *Adv. Funct. Mater.* **2022**, *32*, 2206151.
[4] K. Wang, W. Li, Y. Liao, J. Li, R. Chen, Q. Chen, B. Shi, D. H. Kim, J. H. Park, Y. Zhang, X. Zhou, C. Wu, Z. Liu, T. Guo, T. W. Kim, *Adv. Mater.* **2023**, *35*, 2306065.
[5] H. J. He, L. Jiang, Y. Pan, A. L. Yi, X. H. Zou, W. Pan, A. E. Willner, X. Y. Fan, Z. Y. He, L. S. Yan, *Light: Sci. Appl.* **2023**, *12*, 25.
[6] T. T. Yan, Z. Q. Li, F. Cao, J. X. Chen, L. M. Wu, X. S. Fang, *Adv. Mater.* **2022**, *34*, 2201303.
[7] J. Chen, X. Liu, Z. Li, F. Cao, X. Lu, X. S. Fang, *Adv. Funct. Mater.* **2022**, *32*, 2201066.
[8] X. L. Deng, Z. Q. Li, F. Cao, E. L. Hong, X. S. Fang, *Adv. Funct. Mater.* **2023**, *33*, 2213334.
[9] J. Kim, D. Rhee, O. Song, M. Kim, Y. H. Kwon, D. U. Lim, I. S. Kim, V. Mazanek, L. Valdman, Z. Sofer, J. H. Cho, J. Kang, *Adv. Mater.* **2022**, *34*, 2106110.
[10] X. X. Sun, C. G. Zhu, J. L. Yi, L. Xiang, C. Ma, H. W. Liu, B. Y. Zheng, Y. Liu, W. X. You, W. J. Zhang, D. L. Liang, Q. Shuai, X. L. Zhu, H. G. Duan, L. Liao, Y. Liu, D. Li, A. L. Pan, *Nat. Electron.* **2022**, *5*, 752.
[11] Y. F. Chen, Y. Wang, Z. Wang, Y. Gu, Y. Ye, X. L. Chai, J. F. Ye, Y. Chen, R. Z. Xie, Y. Zhou, Z. G. Hu, Q. Li, L. L. Zhang, F. Wang, P. Wang, J. S. Miao, J. L. Wang, X. S. Chen, W. Lu, P. Zhou, W. D. Hu, *Nat. Electron.* **2021**, *4*, 357.
[12] K. Leng, L. Wang, Y. Shao, I. Abdelwahab, G. Grinblat, I. Verzhbitskiy, R. Li, Y. Cai, X. Chi, W. Fu, P. Song, A. Rusydi, G. Eda, S. A. Maier, K. P. Loh, *Nat. Commun.* **2020**, *11*, 5483.
[13] J. Qiao, F. Feng, S. Song, T. Wang, M. Y. Shen, G. P. Zhang, X. C. Yuan, M. G. Somekh, *Adv. Funct. Mater.* **2021**, *32*, 2110706.
[14] L. T. Liu, L. A. Kong, Q. Y. Li, C. L. He, L. W. Ren, Q. Y. Tao, X. D. Yang, J. Lin, B. Zhao, Z. W. Li, Y. Chen, W. Y. Li, W. J. Song, Z. Y. Lu, G. L. Li, S. Y. Li, X. D. Duan, A. L. Pan, L. Liao, Y. Liu, *Nat. Electron.* **2021**, *4*, 342.
[15] L. Zhang, J. Jiang, Y. Hu, Z. Lu, X. Wen, S. Pendse, R. Jia, G. C. Wang, T. M. Lu, J. Shi, *J. Am. Chem. Soc.* **2022**, *144*, 17588.
[16] R. Frisenda, E. Navarro-Moratalla, P. Gant, D. P. De Lara, P. Jarillo-Herrero, R. V. Gorbachev, A. Castellanos-Gomez, *Chem. Soc. Rev.* **2018**, *47*, 53.
[17] J. R. An, X. Y. Zhao, Y. N. Zhang, M. X. Liu, J. Yuan, X. J. Sun, Z. Y. Zhang, B. Wang, S. J. Li, D. B. Li, *Adv. Funct. Mater.* **2022**, *32*, 2110119.

[18] X. Y. Zhang, Z. Q. Li, T. T. Yan, L. Su, X. S. Fang, *Small* **2023**, *19*, 2206310.
[19] A. G. Ricciardulli, S. Yang, J. H. Smet, M. Saliba, *Nat. Mater.* **2021**, *20*, 1325.
[20] Y. Lei, Y. Li, C. Lu, Q. Yan, Y. Wu, F. Babbe, H. Gong, S. Zhang, J. Zhou, R. Wang, R. Zhang, Y. Chen, H. Tsai, Y. Gu, H. Hu, Y. H. Lo, W. Nie, T. Lee, J. Luo, K. Yang, K. I. Jang, S. Xu, *Nature* **2022**, *608*, 317.
[21] S. Sidhik, Y. Wang, M. De Siena, R. Asadpour, A. J. Torma, T. Terlier, K. Ho, W. Li, A. B. Puthirath, X. Shuai, A. Agrawal, B. Traore, M. Jones, R. Giridharagopal, P. M. Ajayan, J. Strzalka, D. S. Ginger, C. Katan, M. A. Alam, J. Even, M. G. Kanatzidis, A. D. Mohite, *Science* **2022**, *377*, 1425.
[22] Z. Q. Li, E. L. Hong, X. Y. Zhang, M. Deng, X. S. Fang, *J. Phys. Chem. Lett.* **2022**, *13*, 1215.
[23] D. X. Pan, Y. P. Fu, N. Spitha, Y. Z. Zhao, C. R. Roy, D. J. Morrow, D. D. Kohler, J. C. Wright, S. Jin, *Nat. Nanotechnol.* **2021**, *16*, 159.
[24] E. Hong, Z. Li, F. Cao, X. Deng, X. Zhang, X. S. Fang, *Adv. Opt. Mater.* **2023**, *11*, 2301182.
[25] E. Hong, Z. Li, T. Yan, X. S. Fang, *Nano Lett.* **2022**, *22*, 8662.
[26] E. Z. Shi, B. Yuan, S. B. Shiring, Y. Gao, Akriti, Y. F. Guo, C. Su, M. L. Lai, P. D. Yang, J. Kong, B. M. Savoie, Y. Yu, L. T. Dou, *Nature* **2020**, *580*, 614.
[27] C. C. Stoumpos, C. M. M. Soe, H. Tsai, W. Y. Nie, J. C. Blancon, D. Y. H. Cao, F. Z. Liu, B. Traore, C. Katan, J. Even, A. D. Mohite, M. G. Kanatzidis, *Chem* **2017**, *2*, 427.
[28] J. G. Feng, C. Gong, H. F. Gao, W. Wen, Y. J. Gong, X. Y. Jiang, B. Zhang, Y. C. Wu, Y. S. Wu, H. B. Fu, L. Jiang, X. Zhang, *Nat. Electron.* **2018**, *1*, 404.
[29] J. L. Peng, C. Q. Xia, Y. L. Xu, R. M. Li, L. H. Cui, J. K. Clegg, L. M. Herz, M. B. Johnston, Q. Q. Lin, *Nat. Commun.* **2021**, *12*, 1531.
[30] Z. Li, X. Liu, C. Zuo, W. Yang, X. S. Fang, *Adv. Mater.* **2021**, *33*, 2103010.
[31] Y. C. Liu, Y. X. Zhang, X. J. Zhu, Z. Yang, W. J. Ke, J. S. Feng, X. D. Ren, K. Zhao, M. Liu, M. G. Kanatzidis, S. Z. Liu, *Sci. Adv.* **2021**, *7*, eabc8844.
[32] Z. J. Tan, Y. Wu, H. Hong, J. B. Yin, J. C. Zhang, L. Lin, M. Z. Wang, X. Sun, L. Z. Sun, Y. C. Huang, K. H. Liu, Z. F. Liu, H. L. Peng, *J. Am. Chem. Soc.* **2016**, *138*, 16612.
[33] B. S. Zhu, Z. He, J. S. Yao, C. Chen, K. H. Wang, H. B. Yao, J. W. Liu, S. H. Yu, *Adv. Opt. Mater.* **2018**, *6*, 1701029.
[34] S. C. Zhang, Z. Y. Lin, E. Z. Shi, B. P. Finkenauer, Y. Gao, A. J. Pistone, K. Ma, B. M. Savoie, L. T. Dou, *Adv. Mater.* **2021**, *33*, 2105183.
[35] Y. Gao, E. Z. Shi, S. B. Deng, S. B. Shiring, J. M. Snaider, C. Liang, B. Yuan, R. Y. Song, S. M. Janke, A. Liebman-Pelaez, P. Yoo, M. Zeller, B. W. Boudouris, P. L. Liao, C. H. Zhu, V. Blum, Y. Yu, B. M. Savoie, L. B. Huang, L. T. Dou, *Nat. Chem.* **2019**, *11*, 1151.
[36] Y. P. Fu, W. H. Zheng, X. X. Wang, M. P. Hautzinger, D. X. Pan, L. N. Dang, J. C. Wright, A. L. Pan, S. Jin, *J. Am. Chem. Soc.* **2018**, *140*, 15675.
[37] X. J. Zhong, X. J. Ni, S. Sidhik, H. Li, A. D. Mohite, J. L. Bredas, A. Kahn, *Adv. Energy Mater.* **2022**, *12*, 2202333.
[38] J. N. Chen, L. Gan, F. W. Zhuge, H. Q. Li, J. Z. Song, H. B. Zeng, T. Y. Zhai, *Angew. Chem., Int. Ed.* **2017**, *56*, 2390.